Design and Practical Evaluation of Robust Model Predictive Wind Turbine Control

Klein, Andreas; Wintermeyer-Kallen, Thorben; Zierath, János; Kluge, Kevin; Abel, Dirk; Vallery, Heike; Basler, Maximilian

DOI
10.1002/we.70011

Publication date
2025

Document Version
Final published version

Published in
Wind Energy

Citation (APA)
Klein, A., Wintermeyer-Kallen, T., Zierath, J., Kluge, K., Abel, D., Vallery, H., & Basler, M. (2025). Design and Practical Evaluation of Robust Model Predictive Wind Turbine Control. *Wind Energy*, *28*(5), Article e70011. https://doi.org/10.1002/we.70011

Important note
To cite this publication, please use the final published version (if applicable).
Please check the document version above.

Wind Energy

WILEY

RESEARCH ARTICLE OPEN ACCESS

Design and Practical Evaluation of Robust Model Predictive Wind Turbine Control

Andreas Klein[1] | Thorben Wintermeyer-Kallen[1] | János Zierath[2,3] | Kevin Kluge[1] | Dirk Abel[1] | Heike Vallery[1,4] | Maximilian Basler[1]

[1]Institute of Automatic Control, RWTH Aachen University, Aachen, Germany | [2]W2E Wind to Energy GmbH, Rostock, Germany | [3]Chair of Technical Dynamics, University of Rostock, Rostock, Germany | [4]Delft University of Technology, Delft, the Netherlands

Correspondence: Andreas Klein (a.klein@irt.rwth-aachen.de)

Received: 11 July 2024 | **Revised:** 14 January 2025 | **Accepted:** 15 February 2025

Funding: This research was supported by the Federal Ministry for Economic Affairs and Climate Action (BMWK) on the basis of a decision by the German Bundestag in the research project TurboWind with grant number KK5046901CL0.

Keywords: model predictive control | robust control | state estimation | wind turbine control

ABSTRACT

Wind energy is one of the main renewable energy sources in the current energy transition. Due to ever more and ever larger wind turbines (WT), the requirements for WT operation become more complex. Model predictive control (MPC) for WTs shows the potential to handle these requirements and conflicting control objectives in a single optimization-based controller. Recent research has widely investigated MPC for WT in simulation, but mostly lacks experimental validation. This work aims to experimentally validate MPC on a full-scale WT under real conditions. To this end, we combine an extended Kalman filter for nonlinear state estimation with robust linear time-varying MPC. We evaluate the proposed control algorithm in terms of time-domain performance and power curve in simulation. However, the main contribution of this work is the experimental validation on a 3MW WT in Northern Germany with a total duration of 3-h continuous full access of the controller. We were able to demonstrate stable operation of the proposed MPC in the upper partial load regime, transition regime, and lower full load regime, at measured wind speeds between 4.76 and 13.06 m/s, inside and outside the wake shadow of another WT. The power curve determined in simulation shows comparable results to a reference feedback controller. The MPC formulation combines several control objectives in a single optimization problem, yet the tuning effort still remains complex. In future work, we plan to reduce the complexity of the control loop based on this experimentally validated MPC. We provide our experimental data at https://doi.org/10.5281/zenodo.14644908.

1 | Introduction

Driven by the Paris Climate Agreement, renewable energies cover a great share in the current and future energy mix, while the dependence on fossil fuels decreases. Renewable energy already covered 23 % of the gross consumption of energy in the European Union in 2022 [1]. To further enhance energy yield, industry builds ever more and ever larger wind turbines (WTs) [2].

Due to this expansion, requirements for WT operation become more complex [3]. For example, larger WTs are subject to higher structural loads, demanding structural load-reducing operation. In addition, as WTs replace fossil-fuelled power plants, they may need to support the electrical grid in a similar manner [4, 5]. The expansion also calls for low sound emissions of individual WT to ensure social acceptance [4].

These requirements can conflict with each other. Therefore, reports on the major research challenges in wind energy [3–5] even formulate the research goal for WT control to take a holistic view of the system and to use multi-objective control to deal with conflicting objectives. This contrasts the current

industry standard, which operates WTs using multiple single input, single output feedback control loops [6–9].

Model predictive control (MPC) shows the potential to condense multiple control objectives in a single optimization-based controller, thus reducing the complexity of controller tuning and optimally resolving conflicting objectives within constraints. Numerous publications show the strong potential of MPC for WTs, as presented in review papers [10–13]. However, most investigations rely on simulations only.

As one of the few experimental validation studies, Castaignet et al. [14] tested a single-input, single-output frequency-weighted MPC using trailing edge flaps. However, this controller does not control the entire WT but runs in parallel to a nominal WT controller and aims to reduce loads. The experimental evaluation was limited to a Vestas V27 demonstrator WT and gathered in total 10 time series with 2-min length. Sinner et al. [15] tested an MPC on a scaled WT in a wind tunnel testbed. They compared two variants, with and without preview disturbance information. Here, the MPC actuated only the pitch angles, while another underlying feedback loop controlled the generator torque.

Recently, our group showed preliminary experimental results of full-scale testing of MPC on an industrial multimegawatt WT, using both command variables collective pitch angle and generator torque [16–19]. In that test, we tuned the MPC by means of weight scheduling and a strategy to prevent the WT from stalling [16]. The tests were promising but very limited in duration [17, 18]: In total, the proposed MPC was in access for only 90 min, and not continuously, because the controller was not yet able to stabilize WT operation independently. Problems occurred regarding the feasibility of the online optimization problem as well as actuator oscillations at around 4.65 Hz, calling for a more robust controller [19].

Here, we show for the first time a reliable, experimentally validated MPC approach and its performance on the same full-scale WT in the field, namely, the 3MW WT (W2E-120/3.0fc [20]) by Wind to Energy GmbH (W2E) [17, 18]. To resolve the shortcomings of our previous attempt, we reformulated the control algorithms and implemented a robust model predictive controller (R-MPC) to explicitly take uncertainties into account. We let the resulting controller run for 3 h without encountering any adverse events. In the following, we describe modeling, observer design, control, reference generation, tuning, and experimental evaluation.

We provide our experimental data at https://doi.org/10.5281/zenodo.14644908.

2 | Modeling and Control

2.1 | Control Concept

Figure 1B illustrates the control concept applied to the WT (W2E-120/3.0fc [20]), depicted in Figure 1A. An extended Kalman filter (EKF) (Section 2.3) estimates the dynamic states $\mathbf{x}$ of the WT taking into account the current measurements $\mathbf{y}_m$. Using these states $\mathbf{x}$, an R-MPC (Section 2.4) optimizes the commands $\mathbf{u}$ for three different wind speed trajectories, illustrated in Figure 1E.

As we consider both MPC and R-MPC throughout this paper, we address statements for both controllers to the MPC in the following.

We run the proposed algorithms in parallel to the WT automation of W2E, including a reference feedback controller (RC) that generates alternative commands $\mathbf{u}_{rc}$. This RC provides a benchmark, and it also serves as a fallback controller in any fault cases.

Since the proposed MPC does not consider the pitch angles individually, they may drift apart over time. Therefore, a subsequent pitch synchronization controller "θ sync", shown in Figure 1C, synchronizes the pitch angles of the three rotor blades, thus deriving a synchronized input vector $\mathbf{u}_s$. To this end, we feed back the error between each individual pitch angle θ_1, θ_2, and θ_3 and the collective pitch angle $\overline{\theta}$ through a PI-controller and superimpose the result on the pitching rate command $\dot{\overline{\theta}}_{cmd}$ provided by the MPC.

2.2 | WT Model

Figure 1D shows the dynamic WT model based on [21, 22], which we use in both the EKF and the MPC. A rotor-effective wind speed v_w drives the WT, with resulting torques and forces dictated by its aerodynamics. We do not measure the effective wind speed, so we assume it to be constant

$$\dot{v}_w = 0 \tag{1}$$

and refer to the estimation of the wind speed in Section 2.3 and the wind speed trajectories considered in the R-MPC in Section 2.4.3.

The nonlinear aerodynamics are functions of the collective pitch angle $\overline{\theta}$, the angular speed of the hub ω_h, and the relative wind speed v_{rel}, resulting in an aerodynamic torque T_p and thrust force F_t:

$$\begin{aligned} T_p &= 0.5\rho\pi R^2 v_{rel}^3 \omega_h^{-1} c_p(\omega_h, \overline{\theta}, v_{rel}), \\ F_t &= 0.5\rho\pi R^2 v_{rel}^2 c_t(\omega_h, \overline{\theta}, v_{rel}), \end{aligned} \tag{2}$$

with the air density ρ, rotor radius R, power coefficient c_p, and thrust coefficient c_t. We use nonlinear static maps of these power and thrust coefficients, providing them as functions of collective pitch angle $\overline{\theta}$ and the tip-speed ratio $\lambda = \omega_h \cdot R/v_{rel}$.

The aerodynamic thrust F_t causes a fore-aft tower top movement $\{x_t, \dot{x}_t\}$ and a fore-aft collective blade movement $\{\varphi_b, \dot{\varphi}_b\}$, with all three blades condensed using the small-angle approximation. Modeling the rotor and tower with two degrees of freedom (dof) enables a representation of the first two fore-aft eigenfrequencies. The tower top fore-aft velocity $\dot{x}_t$ influences the effective wind speed: $v_{rel} = v_w - \dot{x}_t$.

The aerodynamic torque T_p and generator torque T_g dictate angular accelerations of the drive train components. Modeling the drive train with three dof enables a representation of the first

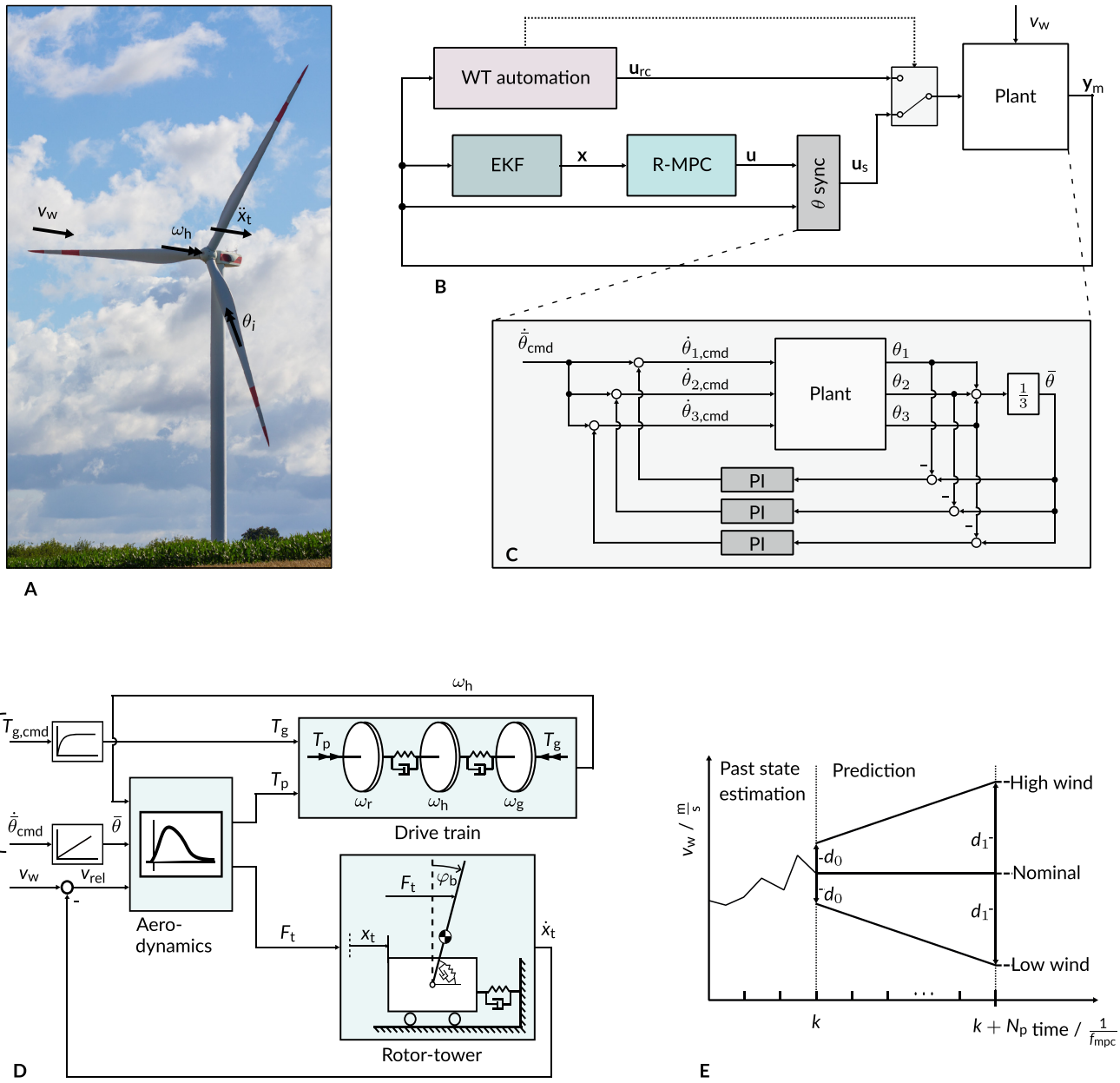

FIGURE 1 | Overview of the WT, control loop, plant model, and considered wind trajectories. (A) The WT (W2E-120/3.0fc [20]) on which we validated our control loop. (B) The proposed feedback control loop. (C) Auxiliary pitch synchronization feedback control loop. (D) WT plant model based on [21, 22] that is used in the EKF and MPC; the subfigure is adapted from [23], licensed under CC BY 4.0. (E) Wind speed trajectories considered in the R-MPC.

two rotational eigenfrequencies and the free rotation. The three angular speeds ω_r, ω_h, and ω_g, respectively, represent rotations of the rotor, hub, and generator in abstract form. The angular differences between rotor and hub as well as hub and generator are denoted as $\Delta\phi_{rh}$ and $\Delta\phi_{hg}$.

All parameters and variables regarding the drive train refer to the low-speed shaft (*lss*), using the gear ratio N_g as a transformation to the high-speed shaft (*hss*):

$$\begin{aligned} T_g &= T_g^{lss} = N_g T_g^{hss}, \\ \omega_g &= \omega_g^{lss} = N_g^{-1} \omega_g^{hss}. \end{aligned} \tag{3}$$

In contrast to [21, 22], we model the generator as a first-order lowpass. Not only do we consider this to be more realistic, but we also avoid a direct feedthrough from the generator torque command $T_{g,cmd}$ to any output, as this caused unstable oscillations in previous experiments. We therefore delay the generator torque command $T_{g,cmd}$ to an actual generator torque T_g. We choose the time constant of the first-order lowpass based on measurement data from the real WT.

Finally, integrating the collective pitching rate command $\dot{\bar{\theta}}_{cmd}$ leads to the collective pitch angle $\bar{\theta}$, neglecting dynamics of the actuator.

As the MPC requires the pitching rate $\dot{\bar{\theta}}$ as output prediction (Section 2.4.2), but we avoid any feedthrough, we define the system state $\bar{\theta}$ to delay the command value by one simulation step.

For the rotor-tower model and the drive train model, we use parameters previously derived by our group [21] through nonlinear optimization based on data obtained from the simulation environment alaska/Wind [24].

We formulate the full system dynamics in discrete-time state-space representation with states $\mathbf{x}$ and inputs $\mathbf{u}$ at time instant k using zero-order hold:

$$\begin{aligned}\mathbf{x}_{k+1} &= \mathbf{A}\mathbf{x}_k + \mathbf{B}\mathbf{w}_k(\mathbf{x}_k, \mathbf{u}_k),\\ \mathbf{u} &= \begin{bmatrix} T_{\mathrm{g,cmd}} & \dot{\bar{\theta}}_{\mathrm{cmd}} \end{bmatrix}^{\mathrm{T}},\\ \mathbf{x} &= \begin{bmatrix} \omega_{\mathrm{r}} & \omega_{\mathrm{h}} & \omega_{\mathrm{g}} & \Delta\phi_{\mathrm{rh}} & \Delta\phi_{\mathrm{hg}} & x_{\mathrm{t}} & \dot{x}_{\mathrm{t}} & \varphi_{\mathrm{b}} & \dot{\varphi}_{\mathrm{b}} & \bar{\theta} & \dot{\bar{\theta}} & T_{\mathrm{g}} & v_{\mathrm{w}} \end{bmatrix}^{\mathrm{T}},\end{aligned} \tag{4}$$

using the discrete-time system matrix $\mathbf{A}$, input matrix $\mathbf{B}$, and virtual input functions $\mathbf{w}$. We condense all nonlinearities in these virtual inputs $\mathbf{w}$.

The symbolic toolbox CasADi [25] allows to generate the Jacobian $\mathbf{J}|_{\mathrm{op}} = \left[\left.\frac{\partial \mathbf{w}_k}{\partial \mathbf{x}_k}\right|_{\mathrm{op}}, \left.\frac{\partial \mathbf{w}_k}{\partial \mathbf{u}_k}\right|_{\mathrm{op}} \right]$ at an operating point *op* automatically using algorithmic differentiation. In contrast to equivalent toolboxes, CasADi is able to differentiate through the numerical maps of c_{p} and c_{t}.

We use this Jacobian to linearize the model in the subsequent control algorithms and thus derive the linearized approximation $\tilde{\mathbf{x}}$,

$$\tilde{\mathbf{x}}_{k+1} = \underbrace{\left[\mathbf{A} + \mathbf{B}\left.\frac{\partial \mathbf{w}_k}{\partial \mathbf{x}_k}\right|_{\mathrm{op}}\right]}_{\mathbf{A}_{\mathrm{lin}}|_{\mathrm{op}}} \mathbf{x}_k + \underbrace{\left[\mathbf{B}\left.\frac{\partial \mathbf{w}_k}{\partial \mathbf{u}_k}\right|_{\mathrm{op}}\right]}_{\mathbf{B}_{\mathrm{lin}}|_{\mathrm{op}}} \mathbf{u}_k, \tag{5}$$

using the linearized state-space matrices $\{\mathbf{A}_{\mathrm{lin}}, \mathbf{B}_{\mathrm{lin}}\}$.

To keep notations simple, we use the general designations $\mathbf{A}$, $\mathbf{B}$, $\mathbf{A}_{\mathrm{lin}}$, and $\mathbf{B}_{\mathrm{lin}}$ for the state-space representation used in both EKF and MPC in the following, although these differ in their sampling frequency.

As the model outputs of the EKF and the MPC differ, we describe the outputs in Sections 2.3.2 and 2.4.2, respectively.

2.3 | EKF State Estimation

2.3.1 | Setup

We follow the EKF algorithm described in [26]. Here, we sample the EKF with a frequency of $f_{\mathrm{ekf}} = 100$ Hz, which is the same as in the underlying WT automation system and 10 times faster than the MPC (Section 2.4).

We perform the nonlinear prediction of the a priori states $\mathbf{x}_{k+1}^{-}$ using the current actuator measurements $\mathbf{u}_{\mathrm{m}}$ instead of the commands $\mathbf{u}$:

$$\mathrm{x}_{k+1}^{-} = \mathbf{A}\mathrm{x}_k + \mathbf{B}\mathrm{w}_k(\mathrm{x}_k, \mathrm{u}_{\mathrm{m},k}). \tag{6}$$

By using the measurements $\mathbf{u}_{\mathrm{m}}$ instead of the control commands $\mathbf{u}$, we aim to achieve a more precise estimation due to the measurements $\mathbf{u}_{\mathrm{m}}$ having a tenfold higher update rate compared to the control commands $\mathbf{u}$ of the MPC.

For safety reasons, the EKF resets if the estimated angular speed ω_{g} or estimated wind speed v_{w} exceeds safety-critical limits. In those cases, the WT automation switches to the RC. When resetting, we use a default covariance matrix $\mathbf{P}_0$ and default initial state vector $\mathbf{x}_0$. We initialize only the effective wind speed v_{w} with the measurement of an anenometer located at the nacelle to support initial convergence of the EKF.

As in [17, 21], we additionally incorporate electrical losses P_{le} and mechanical losses P_{lm} into the model described in Section 2.2 for state estimation. To this end, we use the loss moment T_{L} described in [21], which is a quadratic function of the generator torque T_{g} and generator power $P_{\mathrm{g}} = T_{\mathrm{g}} \cdot \omega_{\mathrm{g}}$,

$$T_{\mathrm{L}} = \frac{1}{\omega_{\mathrm{g}}}\left[\underbrace{a_{\mathrm{e}} P_{\mathrm{g}}^2 + b_{\mathrm{e}} P_{\mathrm{g}} + c_{\mathrm{e}}}_{P_{\mathrm{le}}} + \underbrace{a_{\mathrm{m}} T_{\mathrm{g}}^2 + b_{\mathrm{m}} T_{\mathrm{g}} + c_{\mathrm{m}}}_{P_{\mathrm{lm}}}\right], \tag{7}$$

with the black-box parameters a, b, and c, and indices e for electrical and m for mechanical losses. The black-box parameters were derived empirically and validated using measurement data from the W2E-120/3.0fc.

2.3.2 | Measurements

We utilize the measurement vector $\mathbf{y}_{\mathrm{m}} = \begin{bmatrix} \ddot{x}_{\mathrm{t}}, & \omega_{\mathrm{h}}, & \omega_{\mathrm{g}}, & \bar{\theta}, & T_{\mathrm{g}} \end{bmatrix}^{\mathrm{T}}$ and formulate the prediction of these measurements and the corresponding linearized approximation:

$$\begin{aligned}\mathbf{y}_{\mathrm{m},k} &= \mathbf{C}_{\mathrm{m}}\mathbf{x}_k + \mathbf{D}_{\mathrm{m}}\mathbf{w}_k(\mathbf{x}_k, \mathbf{u}_{\mathrm{m},k})\\ \tilde{\mathbf{y}}_{\mathrm{m},k} &= \underbrace{\left[\mathbf{C}_{\mathrm{m}} + \mathbf{D}_{\mathrm{m}}\left.\frac{\partial \mathbf{w}_k}{\partial \mathbf{x}_k}\right|_{\mathrm{op}}\right]}_{\mathbf{C}_{\mathrm{m,lin}}|_{\mathrm{op}}} \mathbf{x}_k + \underbrace{\left[\mathbf{D}_{\mathrm{m}}\left.\frac{\partial \mathbf{w}_k}{\partial \mathbf{u}_k}\right|_{\mathrm{op}}\right]}_{\mathbf{D}_{\mathrm{m,lin}}|_{\mathrm{op}}=\mathbf{0}} \mathbf{u}_{\mathrm{m},k},\end{aligned} \tag{8}$$

with the measurement and feedthrough measurement matrices $\mathbf{C}_\mathrm{m}$ and $\mathbf{D}_\mathrm{m}$ as well as linearized measurement and feedthrough measurement matrices $\mathbf{C}_\mathrm{m,lin}$ and $\mathbf{D}_\mathrm{m,lin}$. As we avoid any feedthrough from inputs to outputs (Section 2.2), the matrix $\mathbf{D}_\mathrm{m,lin}$ equals zero.

The EKF receives the measurement data of the angular speed of the hub ω_h and generator ω_g, the collective pitch angle $\overline{\theta}$, and the generator torque T_g directly from sensors.

We estimate the fore-aft acceleration data $\ddot{x}_\mathrm{t}$ from an accelerometer installed in the nacelle. We need to preprocess the raw measurements $\ddot{x}_\mathrm{t,m}$ as the accelerometer measures not only translational fore-aft acceleration but also gravitation g depending on the tilt φ of the nacelle:

$$\begin{aligned}\ddot{x}_\mathrm{t,m} &= \cos(\varphi)\cdot\ddot{x}_\mathrm{t} - \sin(\varphi)\cdot g,\\ \tilde{\ddot{x}}_\mathrm{t,m} &= \cos(\varphi_0)\cdot\ddot{x}_\mathrm{t} - \cos(\varphi_0)\cdot g\cdot(\varphi-\varphi_0) - \sin(\varphi_0)\cdot g\end{aligned} \tag{9}$$

using the linearization $\tilde{\ddot{x}}_\mathrm{t,m}$ at $\ddot{x}_\mathrm{t,m,0} = 0$ and $\varphi_0 = \text{constant}$. We do not consider centripetal acceleration as the accelerometer measures tangentially to it.

In order to eliminate the constant term $-\sin(\varphi_0)\cdot g$, which results from an unknown average tilt φ_0 in operation, we high-pass filter the acceleration data. To this end, we use a first-order high-pass filter with a cut-in frequency of 0.5 rad/s, which is lower than all considered eigenfrequencies. We neglect the dynamic error $-\cos(\varphi_0)\cdot g\cdot(\varphi-\varphi_0)$ as well as the factor $\cos(\varphi_0)$, as this appeared small in the high-fidelity simulation of the total value of $\ddot{x}_\mathrm{t}$.

Technically, the anomomenter provides a single-point measurement of the wind speed behind the rotor. However, due to local turbulence, this value differs strongly from the rotor-effective wind speed. In addition, a single-point measurement is generally not well-suited for control [8]. Therefore, following [17, 21], we treat the effective wind speed v_w as an error state without inherent dynamics (1) and rely on state estimation rather than measurement.

2.3.3 | Tuning

We tune the EKF empirically using the simulation environment alaska/Wind [24]. We base the covariance matrix of measurement noise $\mathbf{R}$ on realistic standard deviations of the corresponding sensors. However, we determine the final values of $\mathbf{R}$ as well as the covariance matrix of model noise $\mathbf{Q}$ iteratively in simulation.

We pay special attention to the estimation of the effective wind speed v_w, a key factor for control. The wind speed is the main disturbance but also determines the reference trajectories of the controller. Additionally, the aerodynamic torque T_p and thrust F_t are proportional to the cubic or quadratic effective wind speed, amplifying the wind speed estimation error.

Since we assume constant wind speed (1), the estimation of v_w relies solely on the correction step of the EKF algorithm

$$\mathbf{x}_{k+1}^{+} = \mathbf{x}_{k+1}^{-} + \mathbf{K}_l(\mathbf{y}_{\mathrm{m},k} - \mathbf{y}_{\mathrm{m},k}^{-}), \tag{10}$$

using the a posteriori estimation x^{+} obtained from the prediction error of the measurements $\mathbf{y}_{\mathrm{m},k} - \mathbf{y}_{\mathrm{m},k}^{-}$ and the Kalman Gain $\mathbf{K}_l$. To achieve a fast convergence of the wind speed estimation, we choose a disproportionately high model uncertainty of the wind speed compared to the other states.

2.4 | R-MPC

2.4.1 | Setup

We implement a linear time-varying MPC (LTV MPC) with the adaptive MPC controller from the MathWorks MPC Toolbox [27]. A LTV MPC receives a state-space model in each iteration that is linearized in the current operating point.

The sampling frequency f_mpc and the prediction time T_h are a compromise between computational effort and dynamic requirements. The dynamic requirements result from the minimum and maximum eigenfrequencies f_min and f_max of the model (4). We choose

$$\begin{aligned}f_\mathrm{mpc} &= 10Hz \approx 2.8\cdot f_\mathrm{max},\\ T_\mathrm{h} &= 5s \approx 1.3\cdot f_\mathrm{min}^{-1},\end{aligned} \tag{11}$$

resulting in a prediction horizon of $N_\mathrm{p} = T_\mathrm{h}\cdot f_\mathrm{mpc} = 50$ time samples.

A move-blocking strategy combines a long control horizon with comparatively low computational effort. We therefore choose six optimization input-sets, each of which are active for $\{1, 1, 2, 5, 8, 33\}$ time instants, thus describing all N_p predictions.

We constrain the maximum number of solver iterations in order to limit the computational effort. Based on the CPU load on the programmable logic controller (PLC) (Section 3.1.3), we choose a maximum number of 12 iterations. If the solver exceeds this maximum number, the MPC applies a suboptimal solution.

The MPC resets if the WT operation exceeds safety-critical limits. Whenever the MPC resets or is not in control, the optimized trajectory of the commands starts relative to the current actuator feedback $\mathbf{u}_\mathrm{m}$. During operation, the trajectory starts relative to the last command vector $\mathbf{u}$.

2.4.2 | Output Prediction

We utilize the output vector $\mathbf{y}_\mathrm{p} = \left[\omega_\mathrm{g},\ P_\mathrm{g},\ \overline{\theta},\ \dot{x}_\mathrm{t},\ \dot{\overline{\theta}}_\mathrm{cmd},\ T_\mathrm{g}\right]^\mathrm{T}$ and formulate the prediction of these outputs and the corresponding linearized approximation analogous to (8):

$$\begin{aligned}\mathbf{y}_{\mathrm{p},k} &= \mathbf{C}_\mathrm{p}\mathbf{x}_k + \mathbf{D}_\mathrm{p}\mathbf{w}_k(\mathbf{x}_k,\mathbf{u}_k),\\ \tilde{\mathbf{y}}_{\mathrm{p},k} &= \underbrace{\left[\mathbf{C}_\mathrm{p} + \mathbf{D}_\mathrm{p}\left.\frac{\partial\mathbf{w}_k}{\partial\mathbf{x}_k}\right|_\mathrm{op}\right]}_{\mathbf{C}_{\mathrm{p,lin}}|_\mathrm{op}}\mathbf{x}_k + \underbrace{\left[\mathbf{D}_\mathrm{p}\left.\frac{\partial\mathbf{w}_k}{\partial\mathbf{u}_k}\right|_\mathrm{op}\right]}_{\mathbf{D}_{\mathrm{p,lin}}|_\mathrm{op}=\mathbf{0}}\mathbf{u}_k,\end{aligned} \tag{12}$$

with the output prediction matrices $\mathbf{C}_\mathrm{p}$ and $\mathbf{D}_\mathrm{p}$ as well as linearized output prediction $\mathbf{C}_\mathrm{p,lin}$ and $\mathbf{D}_\mathrm{p,lin}$. As in (8), the linearized

prediction feedthrough matrix $\mathbf{D}_{\mathrm{p,lin}}$ is a zero matrix. We use the predictions $\mathbf{y}_{\mathrm{p}}$ to constrain these and weigh the deviations to their respective reference values (Sections 2.4.4 and 2.4.5).

2.4.3 | Robust Formulation

In order to achieve a robust controller, especially for practical evaluation, we extend the MPC into an R-MPC. To this end, we take into account wind speed uncertainties as the dominant model uncertainty. We therefore extend the prediction of the MPC to a set of three predictions [28] alongside different effective wind speed trajectories

$$
\begin{aligned}
\begin{bmatrix} \mathrm{x}_{k+1} \\ \mathrm{x}^{\mathrm{lw}}_{k+1} \\ \mathrm{x}^{\mathrm{hw}}_{k+1} \end{bmatrix} &= \underbrace{\begin{bmatrix} \mathbf{A} & 0 & 0 \\ 0 & \mathbf{A} & 0 \\ 0 & 0 & \mathbf{A} \end{bmatrix}}_{\mathrm{A_r}} \underbrace{\begin{bmatrix} \mathrm{x}_k \\ \mathrm{x}^{\mathrm{lw}}_k \\ \mathrm{x}^{\mathrm{hw}}_k \end{bmatrix}}_{\mathrm{x}_{r,k}} + \underbrace{\begin{bmatrix} \mathbf{B} & 0 & 0 \\ 0 & \mathbf{B} & 0 \\ 0 & 0 & \mathbf{B} \end{bmatrix}}_{\mathrm{B_r}} \begin{bmatrix} \mathrm{w}_k(\mathrm{x}_k,\mathrm{u}_k) \\ \mathrm{w}^{\mathrm{lw}}_k(\mathrm{x}^{\mathrm{lw}}_k,\mathrm{u}_k) \\ \mathrm{w}^{\mathrm{hw}}_k(\mathrm{x}^{\mathrm{hw}}_k,\mathrm{u}_k) \end{bmatrix}, \\
\begin{bmatrix} \tilde{\mathrm{x}}_{k+1} \\ \tilde{\mathrm{x}}^{\mathrm{lw}}_{k+1} \\ \tilde{\mathrm{x}}^{\mathrm{hw}}_{k+1} \end{bmatrix} &= \underbrace{\begin{bmatrix} \mathbf{A}+\mathbf{B}\left.\frac{\partial \mathrm{w}_k}{\partial \mathrm{x}_k}\right|_{\mathrm{op}} & 0 & 0 \\ 0 & \mathbf{A}+\mathbf{B}\left.\frac{\partial \mathrm{w}^{\mathrm{lw}}_k}{\partial \mathrm{x}^{\mathrm{lw}}_k}\right|_{\mathrm{op}} & 0 \\ 0 & 0 & \mathbf{A}+\mathbf{B}\left.\frac{\partial \mathrm{w}^{\mathrm{hw}}_k}{\partial \mathrm{x}^{\mathrm{hw}}_k}\right|_{\mathrm{op}} \end{bmatrix}}_{\mathrm{A_{r,lin}|_{op}}} \begin{bmatrix} \mathrm{x}_k \\ \mathrm{x}^{\mathrm{lw}}_k \\ \mathrm{x}^{\mathrm{hw}}_k \end{bmatrix} + \underbrace{\begin{bmatrix} \mathbf{B}\left.\frac{\partial \mathrm{w}_k}{\partial \mathrm{u}_k}\right|_{\mathrm{op}} \\ \mathbf{B}\left.\frac{\partial \mathrm{w}^{\mathrm{lw}}_k}{\partial \mathrm{u}_k}\right|_{\mathrm{op}} \\ \mathbf{B}\left.\frac{\partial \mathrm{w}^{\mathrm{hw}}_k}{\partial \mathrm{u}_k}\right|_{\mathrm{op}} \end{bmatrix}}_{\mathrm{B_{r,lin}|_{op}}} \mathrm{u}_k,
\end{aligned}
\tag{13}
$$

$$
\begin{aligned}
\begin{bmatrix} \mathrm{y}_{\mathrm{p},k} \\ \mathrm{y}^{\mathrm{lw}}_{\mathrm{p},k} \\ \mathrm{y}^{\mathrm{hw}}_{\mathrm{p},k} \end{bmatrix} &= \underbrace{\begin{bmatrix} \mathrm{C_p} & 0 & 0 \\ 0 & \mathrm{C_p} & 0 \\ 0 & 0 & \mathrm{C_p} \end{bmatrix}}_{\mathrm{C_r}} \begin{bmatrix} \mathrm{x}_k \\ \mathrm{x}^{\mathrm{lw}}_k \\ \mathrm{x}^{\mathrm{hw}}_k \end{bmatrix} + \underbrace{\begin{bmatrix} \mathrm{D_p} & 0 & 0 \\ 0 & \mathrm{D_p} & 0 \\ 0 & 0 & \mathrm{D_p} \end{bmatrix}}_{\mathrm{D_r}} \begin{bmatrix} \mathrm{w}_k(\mathrm{x}_k,\mathrm{u}_k) \\ \mathrm{w}^{\mathrm{lw}}_k(\mathrm{x}^{\mathrm{lw}}_k,\mathrm{u}_k) \\ \mathrm{w}^{\mathrm{hw}}_k(\mathrm{x}^{\mathrm{hw}}_k,\mathrm{u}_k) \end{bmatrix}, \\
\begin{bmatrix} \tilde{\mathrm{y}}_{\mathrm{p},k} \\ \tilde{\mathrm{y}}^{\mathrm{lw}}_{\mathrm{p},k} \\ \tilde{\mathrm{y}}^{\mathrm{hw}}_{\mathrm{p},k} \end{bmatrix} &= \underbrace{\begin{bmatrix} \mathrm{C_p}+\mathrm{D_p}\left.\frac{\partial \mathrm{w}_k}{\partial \mathrm{x}_k}\right|_{\mathrm{op}} & 0 & 0 \\ 0 & \mathrm{C_p}+\mathrm{D_p}\left.\frac{\partial \mathrm{w}^{\mathrm{lw}}_k}{\partial \mathrm{x}^{\mathrm{lw}}_k}\right|_{\mathrm{op}} & 0 \\ 0 & 0 & \mathrm{C_p}+\mathrm{D_p}\left.\frac{\partial \mathrm{w}^{\mathrm{hw}}_k}{\partial \mathrm{x}^{\mathrm{hw}}_k}\right|_{\mathrm{op}} \end{bmatrix}}_{\mathrm{C_{r,lin}|_{op}}} \begin{bmatrix} \mathrm{x}_k \\ \mathrm{x}^{\mathrm{lw}}_k \\ \mathrm{x}^{\mathrm{hw}}_k \end{bmatrix},
\end{aligned}
\tag{14}
$$

using the modified low wind (*lw*) and high wind (*hw*) state vectors $\mathbf{x}^{\mathrm{lw}}$ and $\mathbf{x}^{\mathrm{hw}}$ and corresponding resulting virtual inputs $\mathbf{w}$, output predictions $\mathbf{y}_{\mathrm{p}}$, and linearized approximations marked with a tilde. The index r denotes the corresponding robust state-space matrices. The initial modified state vectors $\mathbf{x}^{\mathrm{lw}}_0$ and $\mathbf{x}^{\mathrm{hw}}_0$ are equal to the estimation of the EKF $\mathrm{x}_0 = \mathrm{x}^+$, despite the wind speed, which follows artificial trajectories.

Figure 1E qualitatively shows these predicted wind speed trajectories starting at time instant k. We formulate an initial divergence d_0 and a final divergence d_1 as tuning variables. Choosing $d_0 = d_1/2$ and $d_1 = 3.75\%$ of the current rotor-effective wind speed allows to consider an assumed turbulence intensity of 7.5%.

We implement the linear trajectories using nonstationary operating points, thus formulating a constant change of wind speed. We linearize the *lw* and *hw* submodels $\mathbf{A}_{\mathrm{r,lin}}|_{\mathrm{op}}$, $\mathbf{B}_{\mathrm{r,lin}}|_{\mathrm{op}}$, and $\mathbf{C}_{\mathrm{r,lin}}|_{\mathrm{op}}$ at the final values of the *lw* and *hw* wind speed trajectories.

2.4.4 | Reference and Constraints

In order to ensure that the MPC controls the WT stably across the entire operating range, accommodating different control targets [19], we create detailed references based on [16–18].

We therefore define a set of reference trajectories for the generator speed ω_{g}, generator power P_{g} and the corresponding collective pitch angle $\overline{\theta}$ offline, based on $\dot{\omega} \cdot I = T_{\mathrm{p}}$, using (2) and the drive train inertia I. The limitation of the tip-speed ratio λ in c_{p} and c_{t} limits the starting point of the trajectories. The trajectories each converge to static final values depending on the wind speed v_{w}. In the full load regime, we set rated power P_{rated} and rated angular speed ω_{rated} by the corresponding $\overline{\theta}$ according to (2). We create the trajectories separately for accelerating and decelerating, as they converge to the final values from the opposite direction. Figure 2A,B each shows 20 of these trajectories for different wind speeds.

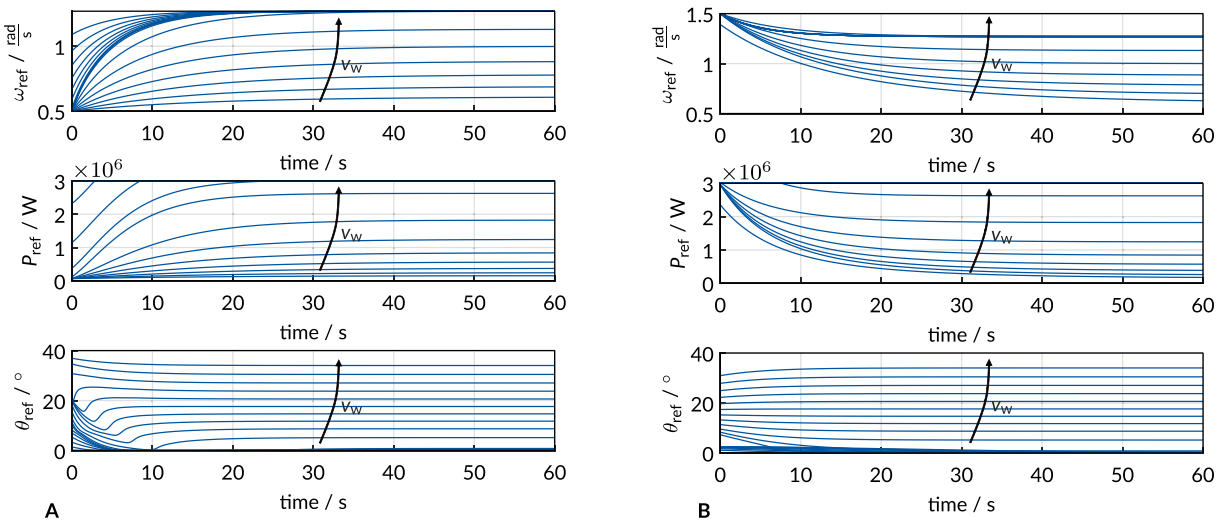

FIGURE 2 | Set of reference trajectories for different wind speeds. (A) Accelerating reference trajectories. (B) Decelerating reference trajectories.

The algorithm identifies the appropriate trajectory online based on the estimated low pass filtered wind speed v_w^+ by means of linear interpolation. It isolates the required subtrajectory of $T_h = 5s$ by identifying the starting point due to the current angular speed ω_g. Eventually, low-pass filtering the pitch trajectory avoids discontinuities of the commands. We raise the power trajectory by a factor of 1.02 to compensate losses. This is a tuning factor.

The reference for the fore-aft tower top velocity $\dot{x}_t$ is zero in order to damp oscillations.

Finally, we use the remaining output predictions of the commands $\dot{\bar{\theta}}$ and T_g to enforce specific behavior regarding the stall region and controller switching to the RC in the experiment. We therefore define a positive pitching rate $\dot{\bar{\theta}}$ that is only active in stall region [16]. Further, we define the reference for the generator torque T_g to be the command torque of the RC but only activate it when switching to the RC to obtain a smooth transition (Section 2.4.5).

Table 1 lists the constraints considered in the MPC. We use the same constraints for the nominal, *lw* and *hw* prediction. The specifications s and h give the type of the constraint, soft (s) or hard (h). We consider all constraints of the commands and command rates as hard constraints to account for actuator limits. In order to avoid infeasibility issues in real-time optimization, we implement soft output constraints. Nevertheless, these soft constraints are more restrictive than the actual shut-down limits of the WT.

2.4.5 | Tuning

We base the MPC tuning on [16]. The cost function of the MPC is defined in [27] and is described textually below.

The cost function penalizes the quadratic deviations of the output prediction vector $\mathbf{y}_p$ to its references, as well as the quadratic values of the commands $\mathbf{u}$ and command rates $\dot{\mathbf{u}}$ in compliance with the constraints.

TABLE 1 | Soft (s) and hard (h) constraints of the optimization problem.

Category	Lower bound	≤	Variable	≤	Upper bound
Output predictions $\mathbf{y}_p$	0	(h)	ω_g	(s)	$\omega_{g,max}$
(same for *lw* and *hw* predictions)	0	(h)	P_g	(s)	$P_{g,max}$
	$\bar{\theta}_{min}$	(s)	$\bar{\theta}$	(h)	$\bar{\theta}_{max}$
Commands $\mathbf{u}$	$\dot{\bar{\theta}}_{min}$	(h)	$\dot{\bar{\theta}}_{cmd}$	(h)	$\dot{\bar{\theta}}_{max}$
	$T_{g,min}$	(h)	$T_{g,cmd}$	(h)	$T_{g,max}$
Command rates $\dot{\mathbf{u}}$	$\ddot{\bar{\theta}}_{min}$	(h)	$\ddot{\bar{\theta}}_{cmd}$	(h)	$\ddot{\bar{\theta}}_{max}$
	$\dot{T}_{g,min}$	(h)	$\dot{T}_{g,cmd}$	(h)	$\dot{T}_{g,max}$

Regarding the output prediction, we weigh the deviation of the references to nominal, *lw* and *hw* prediction. However, we weigh *lw* and *hw* with a factor of 70% compared to nominal, which is a tuning factor.

Table 2 qualitatively shows our tuning, using the tuning parameters p_i, with $i \in \{1, \ldots, 8\}$. Quadratic weight scheduling allows us to handle varying control targets and sensitivities, as well as smooth switching to the RC [16]. We therefore consider the weights q either constant or as functions $f(x)$, depending on the current operating point:

$$f(x) = \begin{cases} q_0 & x \le x_0, \\ q_0 + (x - x_0)^2/(x_1 - x_0)^2 (q_1 - q_0) & x_0 < x \le x_1, \\ q_1 & x_1 < x. \end{cases} \quad (15)$$

TABLE 2 | Applied weight scheduling based on [16].

Weight for		q	x	x_0	x_1	q_0	q_1
$\mathbf{y}_p$	ω_g	$f(x)$	ω_g	ω_{rated}	ω_{max}	$0.25 \cdot p_1$	p_1
	P_g	$f(x)$	$\lvert\omega_g - \omega_{ref}\rvert$	0	$0.1 \cdot \omega_{rated}$	$20 \cdot p_2$	p_2
	$\overline{\theta}$	$f(x)$	v_w	$12\frac{m}{s}$	$9.5\frac{m}{s}$	0	p_3
	$\dot{x}_t$	p_4	—	—	—	—	—
	$\dot{\overline{\theta}}$	$f(x)$	$\overline{\theta}$	$\overline{\theta}_c + 1°$	$\overline{\theta}_c - 10°$	0	p_5
	T_g	$f(x)$	ω_g	$0.95 \cdot \omega_{rated}$	$0.88 \cdot \omega_{rated}$	0	p_6
$\mathbf{u}$	$\dot{\overline{\theta}}_{cmd}$	$f(x)$	$\overline{\theta}$	$\overline{\theta}_c$	$\overline{\theta}_c + 20°$	$0.1 \cdot p_7$	p_7
	$T_{g,cmd}$	0	—	—	—	—	—
$\dot{\mathbf{u}}$	$\ddot{\overline{\theta}}_{cmd}$	0	—	—	—	—	—
	$\dot{T}_{g,cmd}$	p_8	—	—	—	—	—

We penalize the deviation of the angular speed near the maximum speed ω_{max} higher to prevent overspeed. In a situation of high deviations to the references, keeping the desired angular speed is most crucial to prevent the WT from stalling. Therefore, we strongly reduce the weight of the generator power P_g if the angular speed ω_g differs far from its reference ω_{ref}. By scheduling the weight of $\overline{\theta}$, we enable leveraging both commands in the full load regime, while guiding the collective pitch angle $\overline{\theta}$ in the transition regime and partial load regime. We activate the positive reference of $\dot{\overline{\theta}}$ only in the stall region marked by the critical collective pitching angle $\overline{\theta}_c$, where the gradient $\partial c_p / \partial \overline{\theta}$ approaches zero.

Finally, in preparation for smooth switching from the MPC to the RC at a low angular speed, we penalize the deviation from T_g to its reference to enforce the torque command of the RC.

For the commands, we schedule the weight of the $\dot{\overline{\theta}}_{cmd}$ to account for the varying sensitivity of c_p to the collective pitch angle $\overline{\theta}$. We use a constant weight for $\dot{T}_{g,cmd}$.

While we set most weights constant over the prediction horizon, we choose the weight of P_g for only 30 out of $N_p = 50$ time steps, that of $\dot{\overline{\theta}}_{cmd}$ for 10 out of $N_p = 50$ time steps. We set the weights at the remaining time steps to zero. Both result from controller tuning.

3 | Evaluation Procedure

3.1 | Simulation

3.1.1 | Alaska/Wind

We use alaska/Wind [24] to evaluate the state estimation and control results. We run alaska/Wind in co-simulation with Matlab/Simulink, with the interface hosted by a local server [18, 22]. We assume noisy sensor measurements. To this end, we apply white noise with the standard deviation estimated from the real measurements.

As in [22], we evaluate the performance of the EKF in terms of wind speed. This evaluation shows the fundamental issue that the rotor-effective wind speed v_w is a virtual variable without a precise reference. The rotor-effective wind speed v_w is defined as the specific wind speed responsible for rotor and tower acceleration according to (2). We interpret the cubic mean of the wind speed over the rotor surface v_c as the closest reference, due to the cubic relation between power and wind speed.

We evaluate the wind speed estimation in realistic turbulent conditions and synthetic extreme load cases. For this specific purpose, we use a different WT controller that does not rely on the estimation. This way, we do not alter the control results through estimator modification and evaluate solely the estimation.

We show the estimation in three tunings v_w^l, v_w^m, and v_w^h of the EKF that differ only in the covariance of the wind speed noise $q_v \in \{8, 40, 200\}$. In all subsequent evaluations, we use the estimation v_w^m.

Finally, we evaluate the closed-loop control results qualitatively in a time domain plot. To assess the benefit of the robust formulation, we compare the nominal MPC with the R-MPC, which differ solely in the model expansion described in (13) and (14).

3.1.2 | FLEX5

Following [18], we use FLEX5, developed by the Danish Technical University [29], as Software-in-the-Loop (SiL) test stage and to evaluate control results in terms of power production. We compute the power curve according to [30]. As FLEX5 does not compute the cubic mean wind speed v_c, we evaluate the power curves using a single point wind speed simulated at the rotor hub v_h. We intentionally do not base the

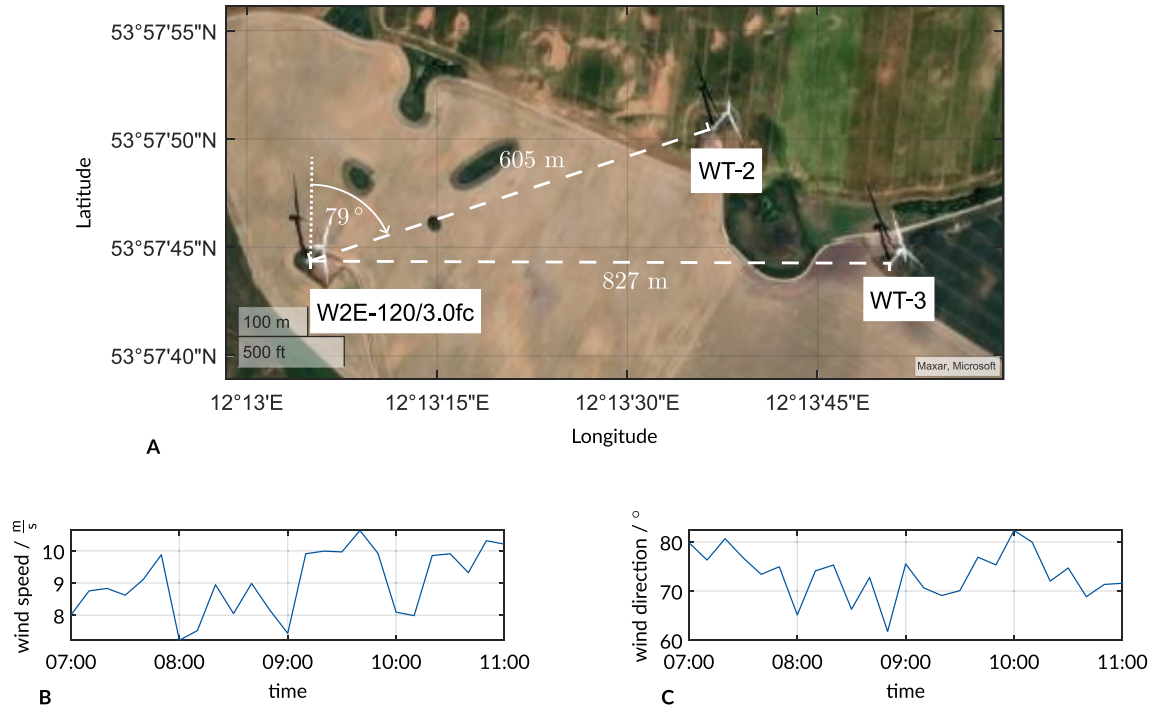

FIGURE 3 | Experimental setup and conditions. (A) W2E wind park, consisting of three WTs, W2E-120/3.0fc, WT-2 and WT-3. (B) Measured wind speed averaged over 10 min. (C) Measured wind direction, clockwise relative to north, averaged over 10 min.

evaluation on the estimated rotor-effective wind speed v_w^+ in order to avoid internal dependency.

The power curve allows us to compare the MPC and the R-MPC with the RC. We use automated code-generation to generate a dynamic-link-library (dll) file and embed it into the WT automation system. For a fair comparison, we do not assume any sensor noise, as the RC does not either.

3.1.3 | Programmable Logic C

We execute the proposed WT feedback control loop comprising the EKF and the MPC on a Bachmann MH230 [31]-PLC under laboratory conditions to evaluate the CPU load on the real PLC. As for the generation of the dll in FLEX5, we use automated code generation. In order to ensure that the control algorithm performs realistically, we feed the controller with realistic process information provided by the plant model (Section 2.2), which we run in parallel.

3.2 | Experiment

3.2.1 | Experimental Setup

We perform the experiment on a W2E-120/3.0fc [20] (3MW-WT). Figure 3A shows the W2E-120/3.0fc in the W2E wind park in Northern Germany, consisting of three WTs, W2E-120/3.0fc, WT-2, and WT-3. WT-2 and WT-3 are located northeast and east of the W2E-120/3.0fc at distances of 605 and 827 m. WT-2 is located at an angle of 79° to W2E-120/3.0fc in relation to north.

The proposed control system using the R-MPC (Section 2.1) runs in parallel to the nominal WT automation from W2E, including the RC. While both controllers are permanently active, the WT automation enables access to the WT depending on the current state. The WT automation also carries out the start and stop procedure. Only in power-production mode the automation system switches to the proposed control loop and only after 60 s to avoid chattering.

We run both the WT automation system and the proposed EKF and R-MPC on a single Bachmann MH230 (Section 3.1.3).

We evaluate the control results of the R-MPC qualitatively in the time domain. In contrast to the simulation, we do not compare the time-domain results with other controllers, because the stochastic nature of the wind speed makes it impossible to reproduce load cases.

However, we compare measurements of the power curve derived with the R-MPC and RC according to [30], using the measured wind speed v_h and measured generator power P_g, both averaged over 10 min. The measurement data of the RC originate from a previous experiment conducted in summer 2023. As we performed the experiments using the R-MPC and RC at different air densities that influence the power as seen in (2), we determine both air densities ρ according to [30] and adjust the measurement data by the corresponding factor.

3.2.2 | Experimental Conditions

We performed the experiment using the R-MPC on December 13, 2023 between 7 and 11 a.m. During this period,

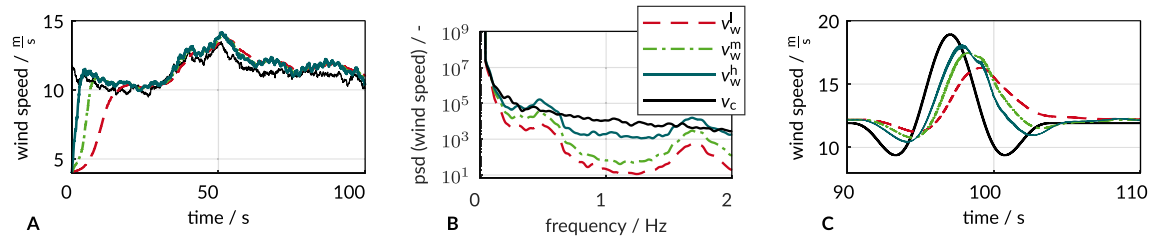

FIGURE 4 | Estimation results in simulation. (A) Estimation of v_w in a turbulent load case in the time domain.(B) Estimation of v_w in a turbulent load case in the frequency domain. (C) Estimation of v_w during an EOG in the time domain.

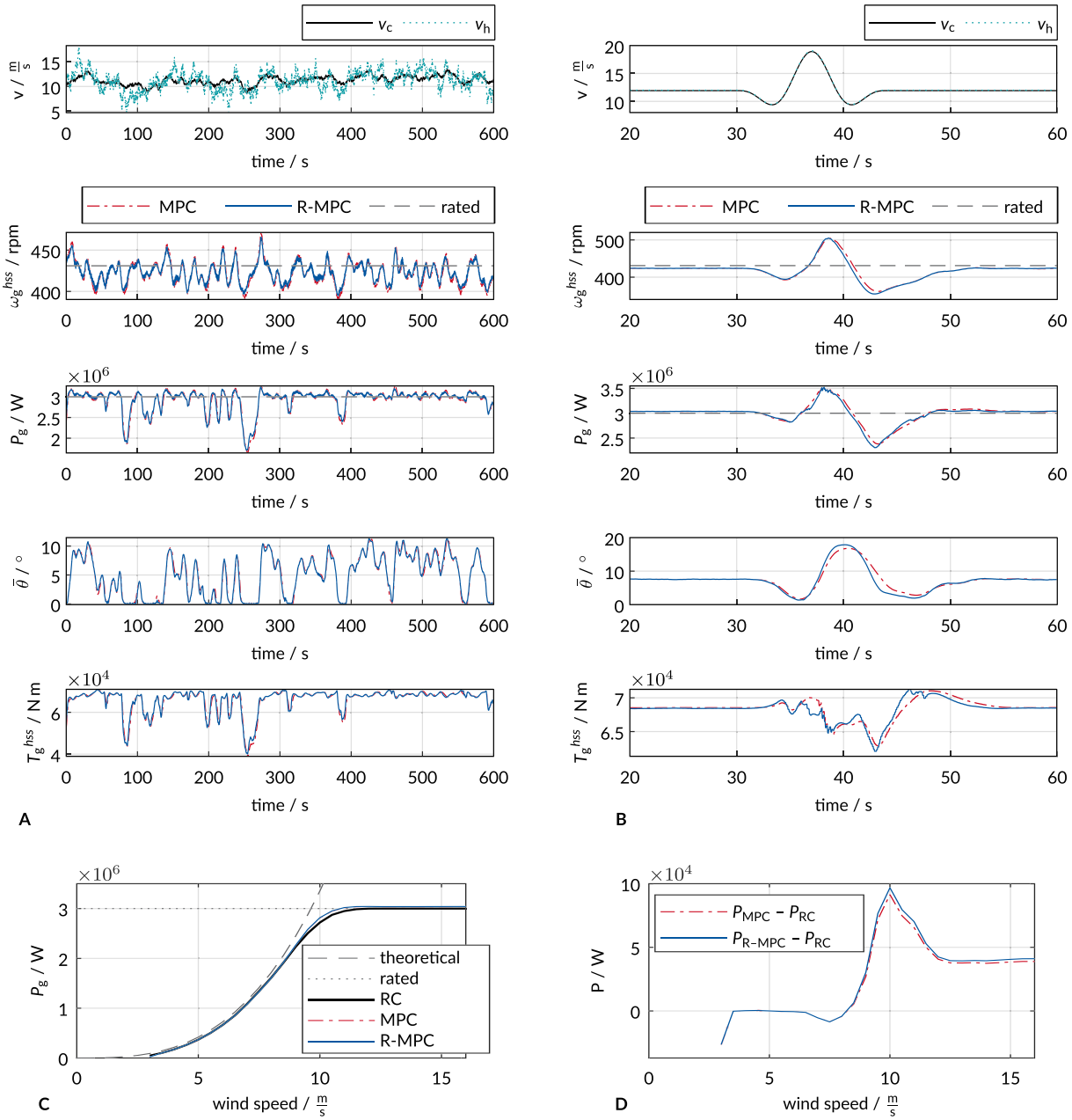

FIGURE 5 | Control results in simulation. (A) Control results of the R-MPC and MPC in a turbulent load case in the transition regime. (B) Control results of the R-MPC and MPC in an EOG. (C) Comparison of power curves in simulation using FLEX5. (D) Power differences of MPC and R-MPC compared to the RC.

the nearest weather station measured an air humidity of 97%, rainfall of 4.3L/m^3, and an air pressure of 1000.3 hPa up to 1001.1 hPa. Figure 3B,C shows the wind speed and wind direction measured in the WT nacelle averaged over 10 min. The temperature measured at the nacelle was at around 2.4°C.

The WT-2 was operating in the morning and stopped at around 10:04 a.m. Due to the north-east wind direction, the W2E-120/3.0fc was mostly behind the WT-2, enabling data acquisition inside and outside its wake shadow, depending on the operation state of WT-2.

4 | Results

4.1 | Simulation Results

Figure 4A,B shows the estimation results of the effective wind speed v_w in a turbulent load case [32] in the time domain and the frequency domain. The frequency-domain plot shows the power spectral density (psd) of a full 10-min time series, starting at 50 s to eliminate the initial convergence phase. The mean wind speed is roughly in the transition regime between partial and full load regime. Figure 4C shows the same configurations in a synthetic *Extreme Operation Gust* (EOG) [32] load case in the time domain.

Figure 5A,B shows the control results in a turbulent load case and an EOG. As for the wind speed estimation, we present the turbulent load case in the transition regime to show the functionality both in partial load regime and full load regime. We display the cubic mean wind speed v_c and hub height wind speed v_h, the controlled variables ω_g and P_g, as well as actuator feedback $\overline{\theta}$ and T_g. We refer ω_g and T_g to hss.

Figure 5C shows the resulting power curves of the WT controlled by MPC, R-MPC and RC in simulation using FLEX5. Figure 5D shows the corresponding power differences of the MPC P_{MPC} and R-MPC $P_{R\text{-}MPC}$, with respect to the RC P_{RC} in detail.

Table 3 shows the CPU load on the Bachmann MH230 [31] when running the MPC, R-MPC, and no controller at all (idle state) for reference. We run the control algorithms on core 2.

4.2 | Experimental Results

We started the WT at 07:44 a.m. The R-MPC was in access from 07:49 a.m. up until the end of the experiment at 10:52 a.m. The optimization problem was feasible during the whole experiment within the maximum number of 12 iterations, and no safety system was triggered.

Figure 6A shows the control results for the entire experiment. As in Figure 5A,B, we present the controlled variables and actuator feedback. In contrast to the simulation results, we show the measured hub height wind speed v_h and the estimated wind speed v_w^+. The measured wind speed v_h was between 4.76 and 13.06 m/s, and the estimated wind speed v_w^+ was between 5.03 and 11.23 m/s.

Figure 6B shows the raw power curve measurement data. The calculated air density of the winter experiment using the R-MPC is 8.7% higher than in the summer experiment using the RC. To mitigate this, Figure 6C presents a comparison with the measurements of R-MPC reduced about a factor of 8.7%.

5 | Discussion

5.1 | Wind Speed Estimation Is a Compromise Between Convergence and Error

In Figure 4A,C, the estimation of the wind speed converges faster if assigned a greater uncertainty. Still, all three displayed estimations seem to converge to the same static values but differ in dynamics. The estimation with high wind uncertainty v_w^h appears to estimate the EOG the fastest and most accurate. Figure 4B indicates, however, that all three estimations of the turbulent wind have increased frequency components at about 0.47 and 1.7 Hz, which the reference cubic wind speed v_c does not exhibit. The estimation using v_w^h shows even higher frequency components at 0.47 and 1.7 Hz compared to v_c.

We explain both with the EKF, which corrects the state vector $\mathbf{x}$ based on the measurement prediction error depending on the Kalman Gain $\mathbf{K}_l$ (10). Here, a disproportionately high uncertainty of the wind speed may cause more errors distributed to v_w, thus inducing incorrect frequency components.

TABLE 3 | CPU load on a Bachmann MH230 [31].

		CPU load / %			
		Core 0	**Core 1**	**Core 2**	**Core 3**
No controller	Mean	~ 1.2	<1	<1	<1
	Maximum	3	2	1	0
MPC	Mean	~ 1.2	<1	~ 7.5	<1
	Maximum	5	3	16	1
R-MPC	Mean	~ 1.2	<1	~ 28	<1
	Maximum	4	4	61	1

These frequency components caused problems in the closed control loop as v_w affects the model, the references, and the weight scheduling. We therefore consider the wind speed estimation as a compromise between convergence speed and dynamic error.

5.2 | MPC Reliably Controls the WT in Different Load Regimes

The time-domain plots in Figure 5A,B show qualitative control results in simulation. The proposed algorithms are able to control the WT in both partial and full load regime in the shown turbulent load case as well as an EOG synthetic load case. Considering the turbulent load case, the R-MPC has lower dynamic amplitudes of the controlled outputs angular speed ω_g and generator power P_g compared to the MPC. We attribute this to the explicit consideration of the uncertainty of the wind speed in the R-MPC. During the EOG, however, the R-MPC exhibits greater dynamic deviations. While we therefore attribute a performance gain in turbulent load cases to the robust formulation, we cannot assume this in general. Figure 5-A,B further indicates static control deviations in the angular speed ω_g and generator power P_g from both R-MPC and MPC. We deduce that previously made assumptions of the electrical and mechanical losses need to be revised or that the various references influence each other.

The power curve and power curve differences shown in Figure 5C,D support the previous discussion. The R-MPC and MPC show comparable results to the RC across the entire operating range. The increased power setpoint of both MPCs, however, is visible in the full load regime in Figure 5D as it is in Figure 5B. The even higher power output of the R-MPC compared to the MPC in the full load regime indicates a shift of the minimum of the cost function of the MPC due to the evaluation for all three predictions nominal, *lw* and *hw*. Finally, the RC uses a "thrust clipping" strategy, where it increases the collective pitch angle $\overline{\theta}$ in the upper part of partial load regime to reduce the maximum thrust. As both MPCs do not address this, a direct comparison in the upper partial load regime provides limited insight.

5.3 | Computational Load Leaves Some Reserve but Is Disproportionately Higher for R-MPC

The CPU load provided in Table 3 shows that both the R-MPC and MPC do not exceed the computational limits of the CPU, but have a reserve. The maximum load of core 2 for both MPCs is about twice as high as the mean. We explain this with the different sample frequencies of the MPC and the remaining algorithms running in parallel.

Moreover, the CPU load of the R-MPC on core 2 is about four times higher compared to the CPU load of the MPC in both the mean and maximum, due to the greater optimization problem. Regarding the control results of the R-MPC and MPC, we find that the proposed robust formulation offers only a marginal improvement relative to the computational effort required.

5.4 | R-MPC Is Able to Control the Real WT Within the Experiment

The experimental results shown in Figure 6 seem to confirm the ability of the R-MPC to ensure stable operation on a real full-scale WT. With a continuous operation time of 3 h, it was our most successful test to date. Due to the experimental conditions, we were able to test a wide operating range of the WT in terms of wind speed. Although gathering results mainly in the upper partial load regime, we were able to collect data in the transition regime and even some in the lower full load regime as well.

In Figure 6A, the measured and estimated wind speeds v_h and v_w seem to have been higher and less turbulent on average as soon as WT-2 stopped at around 10:04 a.m. This operation inside (7:44 a.m up to 10:04 a.m) and outside (10:04 am up to 10:52 a.m.) the wake shadow of WT-2 seems further visible in the angular speed ω_g and power production P_g. This indicates that the R-MPC is able to reliably control the WT in both wind farms and isolation.

Compared to the simulation results in Figure 5A, the measured wind speed v_h appears higher than the estimated wind speed v_w. We explain this with the flow around the nacelle and the associated higher velocity, which is not reflected in the simulation environment alaska/Wind.

The control results in the time domain appear to be comparable to the simulation.

The control results in terms of the adjusted power curve shown in Figure 6C seem to confirm the similarly power output of the WT controlled by the R-MPC and RC. The assumption of different air densities in summer and winter appears to fit the experimental data well, so that the experimental comparison supports the comparison in simulation, shown in Figure 5C.

Finally, both power curves derived from the experiment (Figure 6B,C) seem distorted compared to simulation, due to the difference between the measurement and simulation of the wind speed at hub height v_h.

5.5 | High Model Complexity Leads to High Manual Tuning Effort

Although we are able to combine several control objectives in a single MPC, the proposed methodology consists of a high tuning effort. We identified the model parameters (Figure 1D), tuned the EKF, tuned the R-MPC using weight scheduling, tuned the synchronization controller and created the references. This extensive number of tuning parameters results from the complex requirements for the R-MPC to control the WT stable in the entire operating range, consisting of different control targets in partial load regime and full load regime. Furthermore, this work builds upon the research history [16–19,22], with each successive development tending to increase in complexity to address specific problems.

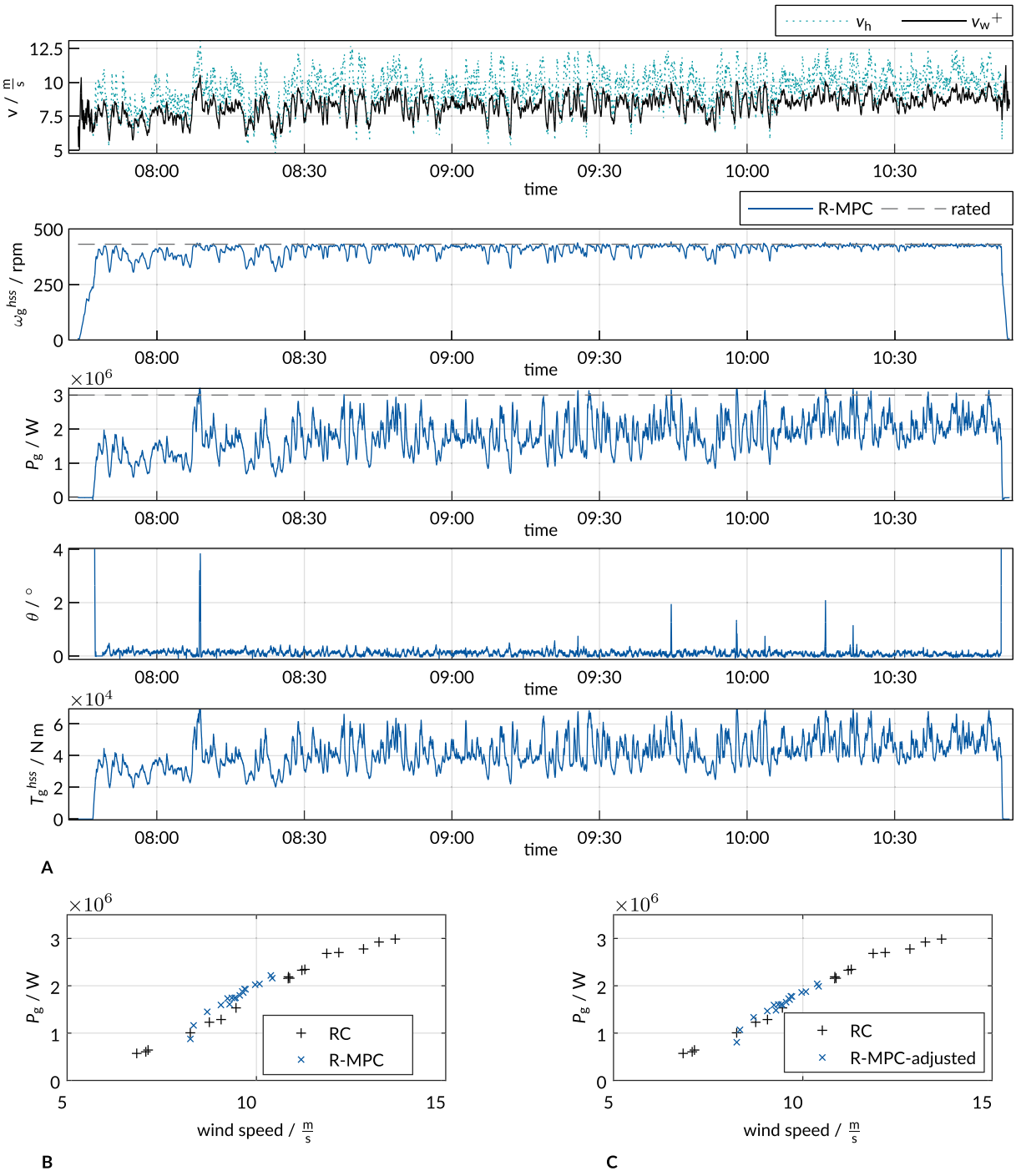

FIGURE 6 | Experimental results. (A) Control results of the proposed control loop in the time domain. (B) Power curve comparison of R-MPC and RC: raw measurement data. (C) Power curve comparison of R-MPC and RC: results of R-MPC adjusted in terms of air density.

We thus cannot yet say that the usage of MPC for WTs reduces the complexity of controller tuning regarding future requirements. On the contrary, we believe that this work paves the way for future research regarding a more practicable, less complex MPC for WTs based on this experimentally validated approach as proof of concept.

5.6 | Future Work

In future work, we plan to reduce the complexity of the algorithms to enhance practicality. We specifically plan to reduce the number of dof of the model, reformulate the losses, and validate the nonrobust MPC in an experiment. In addition, we want

to reduce the complexity of the references to the required minimum and implement a tuning with less parameters. Finally, we plan to explore nonlinear MPC.

At the same time, we plan to explore the integration of some of the initially described requirements such as load reduction, sound limitation, and electrical grid support as extensions into the optimization problem.

6 | Conclusion

The successful experiment indicates the functionality of the proposed R-MPC and EKF for WTs. We were able to test a wide operating range, mainly in partial load regime, transition regime, and lower full load regime, in an unwaked and waked flow field. To the best of our knowledge, we provide the most extensive documented field test with MPC available.

The power curve derived in simulation is comparable to the power curve using the RC. The presented robust formulation of the MPC shows marginal improvement relative to the computational effort, compared to the nonrobust formulation. Concerning wind speed estimation, results indicate a need to compromise between convergence speed and dynamic error.

Despite the positive results, our work did not reduce the complexity of controller tuning regarding future WT control requirement, but instead relied on large engineering effort. We therefore aim for simplification in further research.

Acknowledgments

We would like to thank all colleagues from W2E involved in the MPC test campaign for their help in organizing and supporting the commissioning of the algorithms on their WT and in carrying out the experiment. Open Access funding enabled and organized by Projekt DEAL.

Data Availability Statement

The data that support the findings of this study are openly available in GitHub at https://doi.org/10.5281/zenodo.14644908.

References

1. L. Fernández, "Share of Renewable Energy in the Gross Consumption of Energy in the European Union From 2012 to 2022," (2024).

2. International Renewable Energy Agency (IRENA): Future of Wind: Deployment, Investment, Technology, Grid Integration and Socio-Economic Aspects (a Global Energy Transformation Paper). International Renewable Energy Agency, (2019).

3. G. A. M. van Kuik, J. Peinke, R. Nijssen, et al., "Long-Term Research Challenges in Wind Energy a Research Agenda by the European Academy of Wind Energy," *Wind Energy Science* 1, no. 1 (2016): 1–39, https://doi.org/10.5194/wes-1-1-2016.

4. P. Veers, K. Dykes, R. Baranowski, et al.: Grand Challenges Revisited: Wind Energy Research Needs for a Global Energy Transition. National Renewable Energy Laboratory, (2023).

5. ETIP Wind: Strategic Research & Innovation Agenda 2025-2027. European Technology and Innovation Platform on Wind Energy, (2023).

6. T. Burton, N. Jenkins, D. Sharpe, and E. Bossanyi, *Wind Energy Handbook*, Second Edition, (John Wiley & Sons, 2011).

7. J. Jonkman, S. Butterfield, W. Musial, and Scott, GeorgeJonkman, Jason and Butterfield, Sandy and Musial, Walter and Scott, George, "Definition of a 5-mw reference wind turbine for offshore system development," National Renewable Energy Lab. (Golden, CO (United States), 2009).

8. A. Gambier, *Control of Large Wind Energy Systems: Theory and Methods for the User*, 1st ed., Advances in Industrial Control, (Springer International Publishing and Imprint Springer, 2022).

9. N. J. Abbas, D. S. Zalkind, L. Pao, and A. Wright, "A Reference Open-Source Controller for Fixed and Floating Offshore Wind Turbines," *Wind Energy Science* 7, no. 1 (2022): 53–73, https://doi.org/10.5194/wes-7-53-2022.

10. J. López-Queija, E. Robles, J. Jugo, and S. Alonso-Quesada, "Review of Control Technologies for Floating Offshore Wind Turbines," *Renewable and Sustainable Energy Reviews* 167 (2022): 112787, https://doi.org/10.1016/j.rser.2022.112787.

11. M. Mahmoud and M. Oyedeji, "Adaptive and Predictive Control Strategies for Wind Turbine Systems: A Survey," *IEEE/CAA Journal of Automatica Sinica* 6 (2019): 364–378, https://doi.org/10.1109/JAS.2019.1911375.

12. E. J. Novaes Menezes, A. M. Arajo, and N. S. Bouchonneau da Silva, "A Review on Wind Turbine Control and Its Associated Methods," *Journal of Cleaner Production* 174 (2018): 945–953, https://doi.org/10.1016/j.jclepro.2017.10.297.

13. M. Schwenzer, M. Ay, T. Bergs, and D. Abel, "Review on Model Predictive Control: An Engineering Perspective," *The International Journal of Advanced Manufacturing Technology* 117 (2021): 1–23, https://doi.org/10.1007/s00170-021-07682-3.

14. D. Castaignet, T. Barlas, T. Buhl, et al., "Full-Scale Test of Trailing Edge Flaps on a Vestas v27 Wind Turbine: Active Load Reduction and System Identification," *Wind Energy* 17, no. 4 (2014): 549–564, https://doi.org/10.1002/we.1589.

15. M. Sinner, V. Petrovi, A. Langidis, et al., "Experimental Testing of a Preview-Enabled Model Predictive Controller for Blade Pitch Control of Wind Turbines," *IEEE Transactions on Control Systems Technology* 30, no. 2 (2022): 583–597, https://doi.org/10.1109/TCST.2021.3070342.

16. T. Wintermeyer-Kallen, S. Dickler, J. Zierath, T. Konrad, and D. Abel, "Weight-Scheduling for Linear Time-Variant Model Predictive Wind Turbine Control Toward Field Testing," *Forschung im Ingenieurwesen* 85, no. 2 (2021): 385–394, https://doi.org/10.1007/s10010-021-00475-w.

17. S. Dickler, T. Wintermeyer-Kallen, J. Zierath, et al., "Full-Scale Field Test of a Model Predictive Control System for a 3 mw Wind Turbine," *Forschung im Ingenieurwesen* 85, no. 2 (2021): 313–323, https://doi.org/10.1007/s10010-021-00467-w.

18. S. Dickler. (2022):, "Systematische Entwicklung und Industrienahe Umsetzung ModellprÄdiktiver Regelungen Für Windenergieanlagen," PhD Thesis.

19. T. Wintermeyer-Kallen, M. Basler, T. Konrad, J. Zierath, and D. Abel, "Challenges of Applying Model-Based Predictive Wind Turbine Control in the Field," *Forschung im Ingenieurwesen* 87, no. 1 (2023): 119–128, https://doi.org/10.1007/s10010-023-00634-1.

20. W2E Wind to Energy GmbH, "W2e-120/3.0fc," (2024), Product data sheet.

21. U. Jassmann, S. Dickler, J. Zierath, M. Hakenberg, and D. Abel, "Model Predictive Wind Turbine Control With Move-Blocking Strategy for Load Alleviation and Power Leveling," *Journal of Physics: Conference Series* 753, no. 5 (2016): 052021, https://doi.org/10.1088/1742-6596/753/5/052021.

22. U. Jassmann. (2018):, "Hardware-in-the-Loop Wind Turbine System Test Benches and Their Usage for Controller Validation," PhD Thesis.

23. A. Klein, T. Wintermeyer-Kallen, J. Stegink, et al., "Control-Oriented Wind Turbine Load Estimation Based on Local Linear Neuro-Fuzzy Models," *Journal of Physics: Conference Series* 2767, no. 3 (2024): 032016, https://doi.org/10.1088/1742-6596/2767/3/032016.

24. H. Freudenberg, "Der Einsatz Von Alaska Bei Der Entwicklung Von Windkraftanlagen," Institut für Mechatronik e.V., (2016).

25. J. A. E. Andersson, J. Gillis, G. Horn, J. B. Rawlings, and M. Diehl, "CasADi – A Software Framework for Nonlinear Optimization and Optimal Control," *Mathematical Programming Computation* 11, no. 1 (2019): 1–36, https://doi.org/10.1007/s12532-018-0139-4.

26. S. Haykin, *Kalman filtering and neural networks*, Wiley Series on Adaptive and Learning Systems for Signal Processing, Communications, and Control, (Wiley, 2001).

27. The MathWorks, Inc., "Model Predictive Control Toolbox," (2024).

28. B. Kouvaritakis and M. Cannon, *Model Predictive Control: Classical, Robust and Stochastic*, (Springer International Publishing, 2016).

29. J. Zierath, R. Rachholz, and C. Woernle, "Field Test Validation of Flex5, MSC.ADAMS, Alaska/Wind and Simpack for Load Calculations on Wind Turbines," (2015), https://doi.org/10.1002/we.1892.

30. Deutsches Institut für Normung e.V. (DIN), "DIN EN 61400-12 (VDE 0127-12): Wind Energy Generation Systems - Part 12: Power Performance Measurements of Electricity Producing Wind Turbines - Overview," Beuth Verlag GmbH, Deutsches Institut für Normung e.V. (DIN), (2023).

31. Bachmann electronic GmbH, "Product Data Sheet," (2024).

32. Deutsches Institut für Normung e.V. (DIN), "DIN EN 61400-1 (VDE 0127-1): Wind Energy Generation Systems - Part 1: Design Requirements," Beuth Verlag GmbH, Deutsches Institut für Normung e.V. (DIN), (2019).